A Liquid-Solid Thermo-Mechanical Phase-Field Fracture Model for Electrothermal Wing De-Icing System

Erwann Camberlin, Lokman Bennani, Miguel Charlotte, Eric Paroissien, Michel Salaün

AIAA Aviation Forum and ASCEND co-located Conference Proceedings
29 July - 2 August 2024, Las Vegas, Nevada
AIAA AVIATION FORUM AND ASCEND 2024

A liquid-solid thermo-mechanical phase-field fracture model for electrothermal wing de-icing system

E. Camberlin*
ONERA / DMPE, Université de Toulouse, F-31055, Toulouse, France
Institut Clément Ader (ICA), Université de Toulouse, ISAE-SUPAERO, INSA, IMT MINES ALBI, UTIII, CNRS, F-31400, Toulouse, France

L. Bennani†
ONERA / DMPE, Université de Toulouse, F-31055, Toulouse, France

M. Charlotte‡
Institut Clément Ader (ICA), Université de Toulouse, ISAE-SUPAERO, INSA, IMT MINES ALBI, UTIII, CNRS, F-31400, Toulouse, France

É. Paroissien§
Institut Clément Ader (ICA), Université de Toulouse, ISAE-SUPAERO, INSA, IMT MINES ALBI, UTIII, CNRS, F-31400, Toulouse, France

M. Salaün¶
Institut Clément Ader (ICA), Université de Toulouse, ISAE-SUPAERO, INSA, IMT MINES ALBI, UTIII, CNRS, F-31400, Toulouse, France

This paper addresses the challenge of ice accumulation on aircraft surface wings and focuses on the electrothermal de-icing modeling. Ice buildup on aircraft not only adds weight but also hampers aerodynamic performance, posing a threat to flight safety. Thus, the understanding of ice shedding under the effect of an electrothermal deicer is necessary. However, its modeling remains particularly challenging. This study introduces a novel model utilizing a variational approach, specifically employing phase-field methods. This model incorporates phase change, liquid-solid interaction, and fracture initiation and propagation, allowing for a more enriched multiphysical simulation of the complex electrothermal ice shedding process. The paper provides an overview of existing models, details the chosen modeling of individual phenomena, discusses their coupling, outlines numerical techniques, presents benchmark tests, and concludes with a discussion of results and future prospects.

Nomenclature

b^*	=	Body forces, $m.s^{-2}$
c_0	=	Scaling parameter to recover the shrap crack surface
c_s, c_l	=	Solid and liquid specific heat capacities, $J.kg^{-1}.K^{-1}$
d	=	Damage field
E	=	Young's modulus, Pa
$\mathcal{E}_c$	=	Kinetic energy of the mechanical system, J
$\mathcal{E}_p$	=	Potential energy of the mechanical system, J
f	=	Mixture law function
G_c	=	Critical energy release rate or fracture toughness of the material, $J.m^{-2}$

*PhD Student, Multiphysics department for energy, erwann.camberlin@onera.fr
†Research Engineer, Multiphysics department for energy, lokman.bennani@onera.fr
‡Associate Professor, Department of Mechanical Structures and Materials
§Professor, Department of Mechanical Structures and Materials
¶Professor, Department of Mechanical Structures and Materials

g = Degradation function
h = Enthalpy field, $J.kg^{-1}$
$\mathcal{H}$ = History function field
$\mathbb{I}$ = Identity tensor
J = Heat flux, $W.m^{-2}$
J^* = Boundaries heat flux, $W.m^{-2}$
k_s, k_l = Solid and liquid thermal conductivities, $W.m^{-1}.K^{-1}$
L_{fus} = Latent heat of melting, $J.kg^{-1}$
l_r = Regularized length scale, m
$\mathcal{L}$ = Lagrangian of the mechanical system, J
n = Outward unit normal
$\mathcal{P}$ = External work, J
p^* = External pressure due to aerodynamic forces, Pa
p_L = Liquid layer pressure, Pa
Q^* = Heat source, $W.m^{-3}$
T = Temperature field, K
T^* = External temperature imposed, K
T_0 = Initial temperature, K
T_m = Melting temperature, K
t = Time variable, s
t^* = Boundaries traction forces, Pa
t_{max} = Final time of the simulation, s
u = Displacement field, m
u^* = External displacement imposed, m
$\ddot{u}$ = Acceleration field, $m.s^{-2}$
α = Liquid fraction field
β = Coefficient of thermal expansion, K^{-1}
Γ_c = Sharp crack surface, m^2
Γ_L = Liquid-solid interface, m^2
γ = Crack surface density function
Δ = Laplacian operator, i.e. $\Delta u = \nabla \cdot \nabla u$
Δt = Time step, s
Δx = Average mesh size, m
ϵ = Total strain
ϵ_e = Elastic strain tensor
ϵ_t = Thermal strain tensor
λ = First Lamé coefficient, Pa
μ = Second Lamé coefficient, Pa
ν = Poisson's ratio
ξ = Crack geometric function parameter
ρ = Mass density, $kg.m^{-3}$
σ = Cauchy stress tensor, Pa
σ_S = Solid stress tensor, Pa
σ_L = Liquid stress tensor, Pa
Ψ_c = Surface energy, J
Ψ_e = Stored strain energy, J
$\psi_0^{\pm}$ = Positive / negative (tensile / compressive) parts of the energy density function ψ_0 , $J.m^{-3}$
ω = Crack geometric function
∇ = Gradient operator

I. Introduction

From the earliest days of aviation, the issue of ice accumulation on aircraft has been a recurring problem in the industry [1, 2]. When supercooled water droplets freeze upon contact with an aircraft's surface (such as wings, rotor

blades, etc.), it leads to the buildup of ice layers. This issue not only adds extra weight to aircraft but also significantly impairs their aerodynamic performance, affecting both lift and drag, and posing a considerable threat to flight safety [3]. Numerous systems were developed to prevent the formation of ice or to periodically remove it, including mechanical (e.g., pneumatic or vibratory systems) [4, 5], chemical (de-icers) [6] or thermal (hot bleed-air) [7] systems. One solution that aligns with the ongoing research into more electric aircraft is electrothermal de-icing. This approach involves the installation of heating elements along the aircraft's surface. The fundamental idea, presented in Fig.1 for a wing leading edge, is to allow ice to accumulate and then activate these heating elements. When these elements warm up (for the upper edge: first D, then E and finally F), they create a liquid layer between the aircraft's wing and the ice, weakening the ice's adhesion on the wing surface. Eventually, the aerodynamic forces cause the ice block to detach from its support. This cycle repeats as long as necessary (ice builds up → activation D → activation E → activation F → ice shedding).

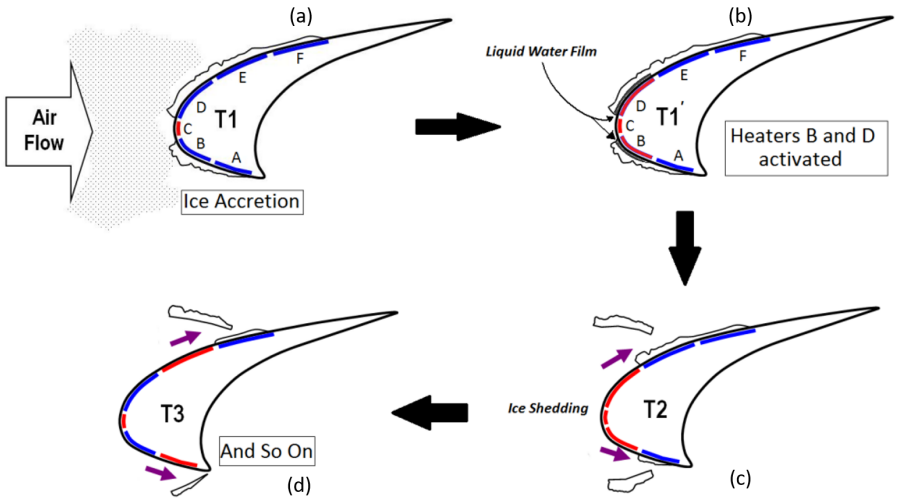

Fig. 1 Electrothermal defrost cycle (Reprinted from [8], ©Elsevier).
(a) The ice builds up; (b) the electrothermal system is activated; (c) a film of water is created between the ice and the wing; (d) the block of ice breaks up and is evacuated.

To comprehensively understand the performance of the de-icing system, it is crucial to explore the process of ice shedding. An empirical criterion, which considers the melting of approximately 80% of the ice block's contact surface [9], is commonly used in industry and academia to assess de-icing success. It is however insufficient to fully grasp the underlying phenomena. Even if this criterion can be verified experimentally and is enough for preliminary system design, it does not take into account the mechanical phenomena leading to ice shedding. Moreover, this criterion does not depend on external parameters, such as external flow for example. Scavuzzo et al. [10] studied the influence of aerodynamic forces on ice shedding using finite elements, concluding that these forces were not negligible. Later, Zhang et al. [11] propose investigating the stress in the ice block caused by aerodynamic forces and the impact on the propagation of a pre-existing crack. However, these works did not consider the thermal aspect of an electrothermal de-icing system. Besides, softwares are developped to simulate and better understand the de-icing phenomena. LEWICE code from NASA [12], Ansys FENSAP-ICE [13] or IGLOO code from ONERA [14] can be cited. None of them realizes a fully coupled model between a mechanical and a thermal part yet. Thus, many questions remain to be answered. What influence does the height of the water film have on the propagation of the crack that allows the ice block to break away? When and where is this crack generated and propagated in the ice? How do the various physical phenomena interact to lead to ice shedding?

Electrothermal ice shedding is a complex process involving various physical phenomena such as aerodynamic flow, solid-to-liquid phase transitions, thermal dynamics, and ice block cracking. This process remains inadequately understood, and its modeling poses numerous challenges. To the best of the authors' knowledge, there is scarce existing research on modeling and simulating the cracking of frost using an electrothermal system. In 2014, Bennani and coworkers [8, 15] aimed to understand the mechanisms leading to fracture in ice and proposed a weak coupling between

a thermal and a mechanical solver. In other fields where similar modeling may be relevant, there are no models that simultaneously account for thermal phenomena including the modeling of phase change and fracture initiation and propagation. In the field of metallurgy, particularly in additive manufacturing, certain models are suggested taking into account some of the mentioned phenomena. One recent article from Ruan et al. [16] includes mechanical aspect with fracture and thermal influence with a damaged-informed heat conduction but without liquid-solid interaction. Another one, from Yeo and Ki [17], consider both thermal effect with phase change, liquid-solid interaction and stress analysis, but without fracture initiation and propagation. In a closer field of study, some researchers are interested in the propagation of crevasses in glaciers, in particular on the influence of the hydrostatic pressure induced by the water present in them. Recent works on crevasses modeling take into account the mechanical aspect with fracture propagation and the solid-liquid interaction, but without any thermal effect (Sun et al. [18], Clayton et al. [19]).

This paper aims to introduce a novel model for simulating frost cracking employing an electrothermal system. To this end, due to the multiphysical aspect of the problem, it was decided to use a variational approach, based in particular on phase-field methods. Phase-field method can be extremely powerful to track the evolution of individual interfaces and allow many physical phenomena to be treated simultaneously. Hence, this novel model uses a phase-field approach while incorporating phase change, liquid-solid interaction and fracture initiation and propagation. These phenomena are coupled in order to take into account the various interactions they may have with each other. This paper is structured as follows. First, an overview of the existing models to simulate the various phenomena is done where the different model choices are presented. Secondly, the chosen modeling of the different phenomena is introduced. First individually, where each model is described without interaction with each other. Then, the coupling between the governing equations is specified. Next, the numerical techniques, such as the numerical implementation, used for the resolution of these equations are addressed. This is followed by some benchmark tests and compared to the literature. Finally the results are discussed. A conclusion and some perspectives of this work complete this paper.

II. Short overview of existing models

In this section, a chronological description of the various events taking place in electrothermal ice shedding is presented. Then, a short overview of existing models for modeling these different phenomena is presented. Lastly, a justification of the models used for this work is brought.

A. Physical phenomena to be modeled

For this work, it is initially assumed that the ice accretion phase has ended and the electrothermal de-icing system is switched off. It results in an ice block attached to the wing surface. The proposed mechanism for electrothermal ice shedding is based on these works [8, 20, 21]. Due to aerodynamic forces, a pressure distribution is applied over the lump. During the activation of the electrothermal de-icing system, a portion of the ice block attached to the wing is warmed and melts into a liquid layer. As illustrated in Fig.2, a surface exists between the external air flow and the liquid layer. It is supposed that the liquid layer is at a hydrostatic pressure equilibrium, and the gravitational effect can be neglected in the fluid. Thus, the pressure of the external flow on the liquid layer is redistributed into it. Because of the ice shape, the flow passing over it is accelerated, driving in a decrease of the pressure on the top ice surface. At the end, the pressure differential between the top ice surface and the liquid layer creates a lifting force, eventually leading to ice shedding.

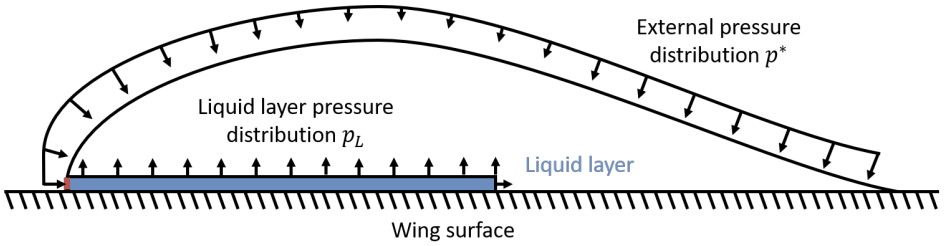

Fig. 2 Schematic pressure distribution on the ice block.

Thus, four phenomena need to be modeled and coupled: 1) the temperature evolution in the ice block, 2) the phase change from solid to liquid due to the electrothermal de-icing system, 3) the mechanical response to pressure distribution

over the ice block and liquid layer and 4) the fracture initiation and propagation.

B. Overview of existing models

When following the chronological sequence of a de-icing cycle, the initial phenomenon to occur is the warming of the ice block, leading to the formation of a liquid layer due to melting. The evolution of the temperature field can be determined classically by solving the heat equation. However, it is crucial to consider that ice undergoes a phase change into liquid water. The thermophysical properties of the medium, such as thermal conductivity and thermal capacity, depend on the phase. Additionally, since the medium comprises two different phases, an interface exists within the domain. In numerical simulations, there are two groups of primary methods for representing an interface between both phases: one group contains front tracking methods and the second group contains front capturing methods [22]. In front tracking methods, the interface is explicitly defined as an internal boundary within the mesh and moves as various quantities change. Thus, it is necessary to solve the heat equation on both sides of the interface (as implemented for de-icing application in ONERA's IGLOO solver [23], which can then also be coupled as a one-way system with a fracture initiation and propagation solver). However, one limitation of these methods is the requirement for the mesh to move with the interface, demanding substantial computational resources for remeshing to maintain high precision when capturing intricate geometries and fine details. On the other hand, front capturing methods define the interface implicitly, reconstructing it using other variables. Often, this reconstruction relies on a variable that varies from 0 to 1 (0 for one phase, 1 for the other, and an intermediate value at the interface). This new variable introduction allows thermophysical properties to vary as a function of the phase. The *Enthalpy-based Method* [9, 24] is an example of front capturing method for phase change modeling. By using the relation between enthalpy and temperature, it is possible to write the energy conservation equation depending only on enthalpy. Solving this equation gives the enthalpy evolution within the studied domain over time. Subsequently, the temperature and liquid fraction fields (and thus the position of the interface) are derived from the enthalpy once the energy equation has been solved. While front capturing methods eliminate the need to remesh the domain to track the interface, they have their own drawbacks. One major limitation is their high dependency on the mesh size for accurate interface positioning, which can lead to high computational costs and complexity, particularly in the presence of rapidly changing or complex interfaces.

As the ice block is melting, the external flow exerts a pressure redistributed into the liquid layer. It is then necessary to model the interaction between the liquid and solid phase, especially how the liquid layer pressure is applied on the solid and how the mechanical stress state evolves. Depending on the method used for the liquid-solid interface modeling, this effect is treated differently. If a front tracking method is used, the liquid-solid interface is explicitly defined. The pressure in the liquid layer is then modeled as a boundary condition of the solid domain, moving as the layer grows, with no need for a stress computation in the liquid domain. If a front capturing method is used, the liquid-solid interface is represented as a diffuse interface without an explicitly defined boundary between both phases. A mixture law must therefore be established to compute the stress in the liquid-solid domain, depending on the parameter describing the current phase of the domain. Similary to the works on hydrofracture [18, 25], the total stress can be split into two parts, each representing the contribution of each phase. From this, the equation of motion can be rewritten on the whole domain, taking into account the liquid and solid phases.

The pressure around the ice block and inside the liquid layer induces a mechanical response of the solid. It leads in the resolution of the equation of motion in the solid domain or liquid-solid domain, depending on the interface modeling choice. This equation can be obtained from a variational formulation of the energy balance of the mechanical system.

Finally, just before ice shedding, a crack is generated and propagates through the ice block. The modeling of cracking dates back to the 1920s, with the work by Griffith [26] who postulated that crack propagation is caused by an energetical balance between elastic energy and crack surface energy. However, his model only deals with crack propagation. Since then, many models were proposed to model crack propagation while including a crack initiation criterion, such as *Continuum Damage Mechanics* from Kachanov [27] leading to *Gradient Damage Model* [28, 29], the *Double Criterion Method* from Leguillon [30] or the *Cohesive Zone Model* from Dugdale and Barenblatt [31, 32]. They do, though, require a prediction of the cracking path. Lastly, a method that has been proving its worth for several years now is the *Phase-Field Model* (PFM) first introduced by Bourdin et al. [33]. The PFM is the numerical application of the works of Francfort and Marigo [34] who deal with the problem as a minimization problem with a variational approach to Griffith's work. The principle is similar to a front capturing method. Instead of representing the crack as a

discontinuity in the solid, a regularization of the crack is made with the introduction of an internal variable (called phase-field variable or damage variable), named d, which represents the damage. This quantity varies from 0 to 1, corresponding with an undamaged material to a fully one respectively. This method is used in a wide range of modeling applications, from ductile to brittle materials and in many different contexts [35].

C. Modeling choices

In the case of electrothermal de-icing, because of the multiphysical context and the need to couple quantities, the choice is made to work with the front capturing method. This choice means that the discontinuities in the problem (liquid-solid boundary, cracking) can be treated as a continuous problem. This also permits a single mesh to be used to solve all of the subproblems, without the need to remesh in order to follow an interface (as would be the case with a front tracking method). Four key variables can describe the defrosting process: the displacement field denoted as u, the damage field represented by d, the temperature field indicated as T, and the liquid fraction field referred to as α.

For thermal modeling, the *Enthalpy-based Method* has been chosen. This choice is justified by its ability to handle both the evolution of the temperature field T and the phase change (liquid fraction field α) through the enthalpy variation in the liquid-solid domain.

Because a front capturing method is used for thermal modeling, the liquid-solid interface is diffuse. Using the liquid fraction field α, it is possible to define a mixture law from liquid stress to solid stress, allowing to solve the equation of motion in the whole liquid-solid domain.

For crack modeling, in the context of electrothermal de-icing application, the method used must be able to calculate the crack initiation and propagation without having any knowledge of the direction of cracking. The choice then naturally falls on the PFM. Coupled with the equation of motion, the resolution of the governing equation given by the PFM provides the evolution of the displacement field u and the damage field d. As the ice is a brittle material, the PFM formulation for brittle materials is used.

To conclude this section, an interconnection diagram, presented in Fig.3, represents the quantities studied and their coupling. For this work, the evolution of the displacement (u), damage (d), temperature (T) and liquid fraction (α) fields of an isotropic thermo-elastic solid and liquid body $\Omega \subset \mathbb{R}^2$, with external boundary $\partial\Omega \subset \mathbb{R}$ over a time period $[0, t_{max}]$ is considered.

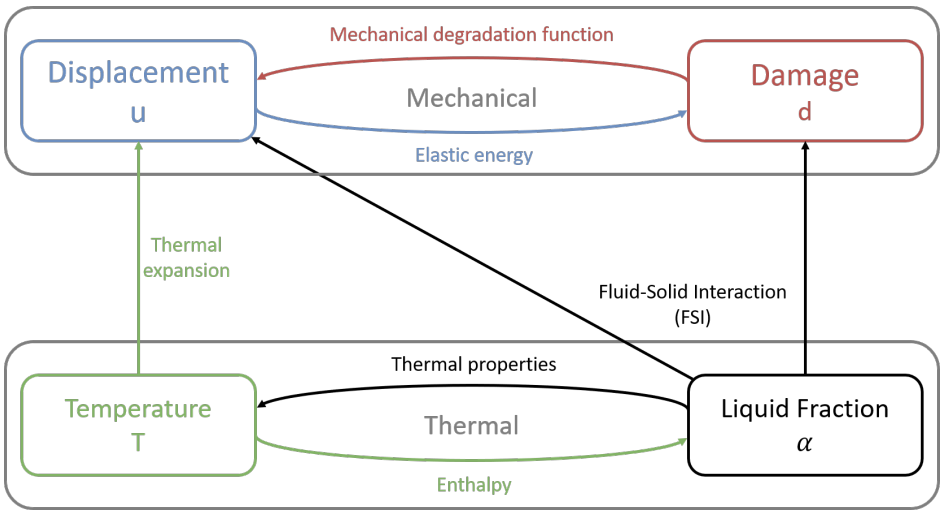

Fig. 3 Interconnection diagram between the different quantities

III. A liquid-solid thermo-mechanical phase-field cracking model

A. Outline

This section introduces the comprehensive liquid-solid thermo-mechanical phase-field cracking model addressed in this paper, which accounts for brittle fracture, thermal effects, phase change and liquid-solid interaction. Initially, the different phenomena are described individually. A presentation and justification are provided for the various equations that constitute the model. Subsequently, these components are merged to form a coupled liquid-solid thermo-mechanical phase-field cracking model, building upon the groundwork laid by the preceding models.

Consider a domain $\Omega \subset \mathbb{R}^2$, presented in Fig.4, composed of two subdomains: a liquid one Ω_L and a solid one Ω_S such that $\Omega_L \cup \Omega_S = \Omega$. In the solid domain Ω_S lies a crack denoted as Γ_c. At the boundary $\partial\Omega_S$ of the solid subdomain Ω_S can be applied Neumann boundary conditions, designed as $\partial_N\Omega_S$, or Dirichlet boundary conditions, noted $\partial_D\Omega_S$. In the same way, the liquid subdomain boundary $\partial\Omega_L$ can be divided into two subsets, $\partial_N\Omega_L$ and $\partial_D\Omega_L$, where Neumann and Dirichlet boundary conditions are imposed, respectively. The liquid and solid domain are separated by an interface, noted Γ_L. For the thermal part, the boundary $\partial\Omega$ is split into $\partial_N\Omega$ and $\partial_D\Omega$ on which heat flux or temperature can be imposed.

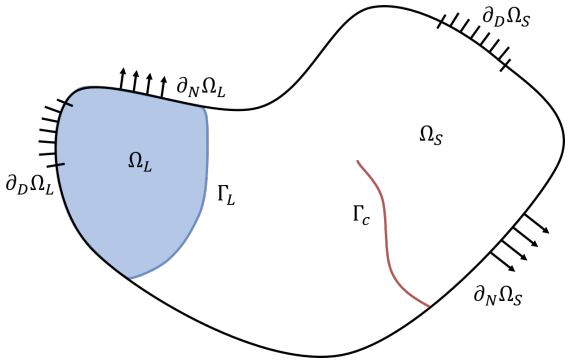

Fig. 4 Schematic of the solid domain Ω_S affected by a crack Γ_c, part of which has melted into a liquid domain Ω_L separated by an interface Γ_L

B. Brittle fracture modeling

First, only the mechanical part of the problem (displacement and damage) is considered. With the same vision as the energetic approach from Griffith [26], which is that crack propagation is a result of the competition between the stored strain energy and the surface energy on the crack, the Lagrangian $\mathcal{L}$ of the mechanical system, as defined by Borden et al. [36], is written as follows:

$$\mathcal{L} = \mathcal{E}_c - \mathcal{E}_p = \mathcal{E}_c - (\Psi_e + \Psi_c - \mathcal{P}) \tag{1}$$

where $\mathcal{E}_c = \int_{\Omega_S} \frac{1}{2}\rho\dot{u} \cdot \dot{u} d\Omega_S$ is the kinetic energy, ρ the mass density, and $\mathcal{E}_p$ the potential energy, which is decomposed into the stored strain energy Ψ_e, the surface energy Ψ_c and the external work $\mathcal{P}$. The external work functional $\mathcal{P}$ can be written as:

$$\mathcal{P}(u) = \int_{\Omega_S} \rho b^* \cdot u d\Omega_S + \int_{\partial_N\Omega_S} t^* \cdot u d\partial_N\Omega_S \tag{2}$$

with b^* the distributed body force and t^* the tractions applied on the system (the superscript * indicates the prescribed quantities). Next, the stored strain energy Ψ_e is defined as:

$$\Psi_e(u, \Gamma_c) = \int_{\Omega_S \setminus \Gamma_c} \psi_0(\epsilon_e(u)) d\Omega_S \tag{3}$$

The elastic strain energy density function $\psi_0(\epsilon_e(u)) = \frac{\lambda}{2}(tr(\epsilon_e))^2 + \mu\,\epsilon_e : \epsilon_e$ is depending on the elastic strain tensor $\epsilon_e(u) = \frac{1}{2}(\nabla u + \nabla u^T)$ and the Lamé coefficients λ and μ. Finally, the surface energy Ψ_c is defined as:

$$\Psi_c(\Gamma_c) = \int_{\Gamma_c} G_c d\Gamma_c \tag{4}$$

where G_c is the critical energy release rate, also called the fracture toughness, which is a material property.

Following the works of Francfort and Marigo [34], then from Bourdin et al. [33], the surface energy is approximated as:

$$\Psi_c(\Gamma_c) \approx \Psi_c(d) = \int_{\Omega_S} G_c \gamma(d, \nabla d) d\Omega_S \tag{5}$$

where a crack surface density functional $\gamma(d, \nabla d)$ is introduced, depending on the damage variable $d \in [0, 1]$. The region with $d = 0$ and $d = 1$ correspond to undamaged and fully broken states of the material. Due to the regularization of the sharp crack, the stored strain energy is modified:

$$\Psi_e(u, d) = \int_{\Omega_S} \psi(\epsilon_e(u), d) d\Omega_S \tag{6}$$

The stored energy functional $\psi(\epsilon_e(u), d)$ describes a smooth transition from the undamaged bulk material to the fully crack state, characterised by the initial free energy density function $\psi_0(\epsilon_e(u))$ and a degradation function $g : d \to g(d) : [0, 1] \to [1, 0]$. In order to prevent cracking in regions under compression, a tension/compression split of $\psi_0(\epsilon_e(u))$ is performed such that:

$$\psi(\epsilon_e(u), d) = g(d)\psi_0^+(\epsilon_e(u)) + \psi_0^-(\epsilon_e(u)) \tag{7}$$

where the degradation function $g(d)$ is only applied to what contributes to cracking (tensile part). The choice is made to use a spherical / deviatoric decomposition to calculate $\psi_0^{\pm}$. This decomposition was first used in the context of phase-field by Lancioni and Royer-Carfagni in the study of failures of some structural parts of the French Panthéon [37].

From the lagrangian $\mathcal{L}$ presented previously and with the definition of each energy, it is possible to search u and d, such that they are verifying the associated Euler-Lagrange equations describing the mechanical evolution of the system:

$$\nabla \cdot \sigma_S + \rho b^* = \rho \ddot{u} \quad \text{in} \quad \Omega_S \times [0, t_{max}] \tag{8a}$$

$$\sigma_S \cdot n = t^* \quad \text{on} \quad \partial_N \Omega_S \times [0, t_{max}] \tag{8b}$$

for the displacement subproblem, where σ_S is the solid stress tensor defined by the Hooke law: $\sigma_S(\epsilon_e) = \lambda tr(\epsilon_e)\mathbb{I} + 2\mu\epsilon_e$. Due to the weak motion of the system, the inertia part of the displacement equation is neglected in the remainder of this paper.

The damage subproblem governing equations are also derived:

$$G_c \left(\frac{\partial \gamma}{\partial d} - \nabla \cdot \frac{\partial \gamma}{\partial \nabla d} \right) = -\frac{\partial \psi}{\partial d} \quad \text{in} \quad \Omega_S \times [0, t_{max}] \tag{9a}$$

$$\frac{\partial \gamma}{\partial \nabla d} \cdot n = 0 \quad \text{on} \quad \partial_N \Omega_S \times [0, t_{max}] \tag{9b}$$

Wu et al. [38] proposed a general form for the crack surface density function:

$$\gamma(d, \nabla d) = \frac{1}{c_0} \left[\frac{1}{l_r} \omega(d) + l_r |\nabla d|^2 \right] \tag{10}$$

caracterized by a geometric crack function $\alpha(d)$, a scaling parameter $c_0 = 4 \int_0^1 \sqrt{\omega(y)} dy$ and a regularized length l_r. As the length scale l_r approaches to zero, the regularized crack surface converges to the sharp crack. The geometric crack function is taken as:

$$\omega(d) = \xi d + (1 - \xi) d^2 \in [0, 1] \quad \forall d \in [0, 1] \tag{11}$$

for $\xi \in [0, 2]$, which is a parameter used to select the cracking model. If $\xi = 0$, the Bourdin's et al. model [33], also known as the AT2 model, is reverted to, employing a quadratic geometric crack function $\alpha(d) = d^2$. Its linear counterpart $\alpha(d) = d$ can be found with $\xi = 1$ to correspond to Pham's et al. model [39] (also called AT1 model). If the expression of γ is introduced in the damage subproblem governing equations, they become:

$$\frac{G_c}{c_0}\left(\frac{1}{l_r}\omega'(d) - 2l_r\Delta d\right) = 2(1-d)\psi_0^+(\epsilon_e) \quad \text{in} \quad \Omega_S \times [0, t_{max}] \tag{12a}$$

$$\nabla d \cdot n = 0 \quad \text{on} \quad \partial_N\Omega_S \times [0, t_{max}] \tag{12b}$$

In the remainder of this paper, the AT2 model is adopted.

However, in this current form the damage variable d can decrease, leading to a "healing" of the material. To take into account the irreversibility process of fracture, Miehe et al. [40] introduce a history function $\mathcal{H}$ defined as:

$$\mathcal{H} = \max_{0 \le t' \le t}\left(0, \psi_0^+(\epsilon_e(\mathbf{x}, t'))\right) \tag{13}$$

The new governing equations for the damage subproblem become:

$$\frac{G_c}{c_0}\left(\frac{1}{l_r}\omega'(d) - 2l_r\Delta d\right) = 2(1-d)\mathcal{H} \quad \text{in} \quad \Omega_S \times [0, t_{max}] \tag{14a}$$

$$\nabla d \cdot n = 0 \quad \text{on} \quad \partial_N\Omega_S \times [0, t_{max}] \tag{14b}$$

Thus, the damage can not now decrease through time and the irreversibility process is respected.

C. Thermo-mechanical model

The thermal problem is now introduced. First, the thermal strain tensor ϵ_t, which represents the thermal expansion of the solid due to temperature change, is defined as:

$$\epsilon_t = \beta(T - T_0)\mathbb{I} \tag{15}$$

where β is the thermal expansion coefficient of the material, T_0 the initial temperature, T the actual temperature and $\mathbb{I}$ the identity tensor. This leads to a change in the definition of the elastic strain in the solid. The elastic strain ϵ_e is now defined as the difference of the total strain ϵ and the thermal strain, such that:

$$\epsilon_e = \epsilon - \epsilon_t = \frac{1}{2}(\nabla u + \nabla u^T) - \beta(T - T_0)\mathbb{I} \tag{16}$$

The definition of the elastic strain density function $\psi(\epsilon_e, d)$ and the stress tensor $\sigma(\epsilon_e, d)$ is modified accordingly.

Secondly, to calculate the temperature evolution in the domain, let us consider the thermal energy conservation equation:

$$\frac{\partial \rho h}{\partial t} + \nabla \cdot J = Q^* \tag{17}$$

where ρ is the mass density, h is the specific enthalpy, J is the heat flux and Q a potential body heat source. Introducing the liquid fraction α for the definition of h, the specific enthalpy is related to the temperature T through the following relation:

$$h = \begin{cases} c_s(T - T_m) & \text{In solid phase } \ T < T_m \\ \alpha L_{fus} & \text{At liquid-solid interface } \ T = T_m \\ c_l(T - T_m) + L_{fus} & \text{In liquid phase } \ T > T_m \end{cases} \tag{18}$$

where $c_{s,l}$ is the specific heat capacity of the solid/liquid phase. In this work, thermal conduction is the only phenomenon treated as a heat exchange. Thus, the heat flux J obeys the Fourier law: $J = -k\nabla T$, where k is the thermal conductivity of the material.

To take into account the phase change phenomenon, this thermal energy equation needs to be solved in both the liquid and solid domain. Thermal properties should also depend on the current phase. The specific heat capacity c

is already covered by the specific enthalpy definition. All that is left is to define the thermal conductivity k as being dependent on the liquid fraction α. Considering the thermal capacity in the liquid is k_l, and in the solid it is k_s, one defintion could be:

$$\frac{1}{k(\alpha)} = \frac{(1-\alpha)}{k_s} + \frac{\alpha}{k_l} \tag{19}$$

The governing equations for the thermal subproblem are now:

$$\frac{\partial \rho h}{\partial t} + \nabla \cdot (-k(\alpha)\nabla T(h)) = Q^* \quad \text{in} \quad \Omega \times [0 - t_{max}] \tag{20a}$$

$$J \cdot n = J^* \quad \text{in} \quad \partial_N \Omega \times [0 - t_{max}] \tag{20b}$$

Solving these equations gives the specific enthalpy field h, which can be used to calculate the temperature field T. From the temperature, the new liquid fraction field α is derived:

$$\alpha = \begin{cases} 0 & \text{In solid phase } \ T < T_m \\ \frac{h}{L_{fus}} & \text{At liquid-solid interface } \ T = T_m \\ 1 & \text{In liquid phase } \ T > T_m \end{cases} \tag{21}$$

D. Liquid-solid interaction

The liquid-solid interface is characterized as a diffuse interface and is quantified by the liquid fraction α. The objective is to determine a mixture law for calculating displacement within the liquid phase. The solid stress tensor σ_S has already been established via Hooke's law (as discussed earlier). For the liquid phase, we assume quasi-static conditions and disregard viscous effects. Consequently, the liquid stress tensor σ_L is formulated as:

$$\sigma_L = -p_L \mathbb{I} \tag{22}$$

with p_L the pressure in the liquid domain. The following mixture law to calculate the stress in the liquid-solid domain is introduced:

$$\sigma = f(\alpha)\sigma_S + (1 - f(\alpha))\sigma_L \tag{23}$$

Here, the function f denotes the transition from the solid to the liquid phase. Certain conditions must be satisfied by this function. Firstly, when $\alpha = 0$, f should equal 1 since only the solid phase exists, leading to $\sigma = \sigma_S$. Conversely, when $\alpha = 1$, f should equal 0 as only the liquid phase is present, resulting in $\sigma = \sigma_L$. The function $f(\alpha) = (1-\alpha)^2$ is compliant with both conditions and is chosen. As the degradation function g represents a transition between a undammaged and a fully damage state, here taking the mixture function f as the same form sounds interesting. The governing equation for the displacement subproblem is now defined across the entire domain Ω:

$$\nabla \cdot (f(\alpha)\sigma_S + (1 - f(\alpha))\sigma_L) + \rho b^* = 0 \quad \text{in} \quad \Omega \times [0, t_{max}] \tag{24a}$$

$$(f(\alpha)\sigma_S + (1 - f(\alpha))\sigma_L) \cdot n = t^* \quad \text{on} \quad \partial_N \Omega \times [0, t_{max}] \tag{24b}$$

Following this modification of the displacement equations, the damage equation is also affected by the new definition of the stress tensor. The elastic strain energy density is now defined as:

$$\psi(u, d, T) = f(\alpha)\Big(g(d)\psi_0^+(u, T) + \psi_0^-(u, T)\Big) - \Big(1 - f(\alpha)\Big)p_L tr(\epsilon)\mathbb{I} \tag{25}$$

This formulation of the elastic strain energy closely resembles the approaches adopted by Sun et al. and Clayton et al. [18, 25] about modeling fracture propagation in glaciers. However, a key distinction lies in utilizing the liquid fraction α instead of the damage d within the mixture law. With this revised formulation of the elastic strain energy density, the damage equation transforms into:

$$\frac{G_c}{c_0}\left(\frac{1}{l_r}\omega'(d) - 2l_r\Delta d\right) = 2f(\alpha)(1-d)\mathcal{H} \quad \text{in} \quad \Omega \times [0, t_{max}] \tag{26a}$$

$$\nabla d \cdot n = 0 \quad \text{on} \quad \partial_N \Omega \times [0, t_{max}] \tag{26b}$$

If $\alpha = 0$ (solid phase), the equations fall back on those presented above (eq. 8 and eq. 9).

IV. Numerical implementation

In this section, the numerical implementation of the model is presented, featuring discretization with finite elements, resolution of the thermal part using a Newton algorithm, and a staggered approach for the mechanical component. The thermal component is addressed through the utilization of a Newton algorithm, providing an iterative and efficient method for solving the nonlinear equations inherent in heat transfer and phase change processes. Simultaneously, the mechanical aspect is handled through the application of a staggered approach, allowing for a segregated yet synchronized treatment of mechanical and thermal aspects in a staggered time-stepping manner. This amalgamation of techniques aims at the establishment of a numerical framework for the simulation of the intricate interplay between thermal and mechanical phenomena within the model. An in-house code called ROMEA.jl was developped using the Bcube.jl library from ONERA [41].

A. Weak formulation of the equations

The weak form of the presented equations are obtained by multiplying these equations by a set of test functions $\{v_u, v_d, v_T\}$ and integrating over the domain Ω. The weak form for the displacement equation (eq. 8) is:

$$\begin{aligned}\int_\Omega f(\alpha)\Big(g(d)\ \sigma^+(u) + \sigma^-(u)\Big) : \epsilon(v_u)\, d\Omega = \int_\Omega f(\alpha)\Big(g(d)\ \sigma_t^+(T) + \sigma_t^-(T)\Big) : \epsilon(v_u)\, d\Omega \\ + \int_\Omega \Big(1 - f(\alpha)\Big) p_L \mathbb{I} : \epsilon(v_u)\, d\Omega + \int_\Omega \rho b^*\ v_u\, d\Omega + \int_{\partial_N\Omega} t^* v_u\, d\partial_N\Omega\end{aligned} \tag{27}$$

The same procedure is applied on the damage equation (eq. 9):

$$\int_\Omega \frac{2G_c l_r}{c_0}\ \nabla d \cdot \nabla v_d\, d\Omega + \int_\Omega \left(\frac{2G_c}{c_0 l_r} + 2f(\alpha)\mathcal{H}\right) d\ v_d\, d\Omega = \int_\Omega 2f(\alpha)\mathcal{H}\ v_d\, d\Omega \tag{28}$$

Finally, the weak form of the thermal equation is obtained (eq. 20):

$$\int_\Omega \rho\dot{h}\ v_T\, d\Omega + \int_\Omega k(h)\nabla T(h)\ \nabla v_T\, d\Omega = \int_\Omega Q^*\ v_T\, d\Omega + \int_{\partial_N\Omega} J^*\ v_T\, d\partial_N\Omega \tag{29}$$

B. Treatment of boundaries conditions

At the outset of the process, the ice block adheres to the wing, symbolized numerically as a Dirichlet condition applied to the wing-fixed edge. As the de-icing progresses, the ice melts into water. Unlike ice, water is not considered bound to the wing's surface. Consequently, the Dirichlet condition must be replaced by a Neumann condition, representing the external pressure on the liquid layer. The initial Dirichlet condition in equation 8 can then be substituted with a Fourier-Robin boundary condition:

$$\sigma \cdot n + a\ u = b\ p_L \mathbb{I} \cdot n \tag{30}$$

where a and b define an attached or unattached state. If the boundary is in solid state (ice), a is set to a large number and b is set to 0, resulting into a pseudo-Dirichlet condition. If the boundary is in liquid phase (water), a is set to 0 and b to 1, resulting into a Neumann condition.

C. Choice and use of solvers

At the start of the iteration n (at time t^n), the thermal part is first solved in order to obtain the temperature field in the domain and determine the potential melted regions. A semi-implicit Euler method (or Backward Euler method) is used. This lead to solving a non-linear thermal equation. Thus, the following equation is solved:

$$r^{n+1} = \int_\Omega \rho\dot{h}^{n+1} v_T\, d\Omega + \int_\Omega k(h^n)\nabla T(h^{n+1})\nabla v_T\, d\Omega - \int_\Omega Q^* v_T\, d\Omega - \int_{\partial_N\Omega} q^* v_T\, d\partial_N\Omega = 0 \tag{31}$$

Due to the complexity of the coupled equations and the difficulty of solving them, a Courant-Friedrichs-Lewy (CFL) condition is unwanted. Moreover, melting is a slow process, and with the relatively comparable conductivities of water and ice (0.6 $\mathrm{W.m^{-1}.K^{-1}}$ for water and 2.3 $\mathrm{W.m^{-1}.K^{-1}}$ for ice), the error incurred at each iteration will remain relatively minor.

A classical Newton-Raphson method is used to find the solution vector h^{n+1} of the thermal equation in matrix form:

$$M_T \ \frac{h^{n+1} - h^n}{\Delta t} + K_T^n \ T(h^{n+1}) - L_T^n = R^{n+1} \tag{32}$$

The equation is deemed solved when $||R^{n+1}||_\infty < \eta_T$, where η_T represents a small value (usually 10^{-9} in this context). Once the enthalpy field h^{n+1} is derived for time t^{n+1}, the temperature field T^{n+1} and the liquid fraction field α^{n+1} are updated in accordance with their definitions for computing the displacement field u^{n+1} and the damage field d^{n+1}.

The PFM formulation establishes that damage d is driven by the tensile component of elastic strain energy, depending upon the displacement field u. Furthermore, the Cauchy stress tensor relies on the damage field d to determine the displacement field u. Consequently, these two fields are intricately interlinked, forming a strong coupling. For solving such problems, a staggered scheme is preferable, offering flexibility and stability over a monolithic scheme, albeit with a slower convergence rate [35]. The staggered algorithm employed in this study follows that of Miehe et al. [40] and comprises three stages, iterated until convergence. Initially, with the temperature field determined, the displacement field u_{i+1}^{n+1} can be computed using the damage variable d_i^{n+1} from the preceding staggered step, solving the following equation:

$$\begin{aligned}\int_\Omega f(\alpha^{n+1})\Big(g(d_i^{n+1})\ \sigma^+(u_{i+1}^{n+1}) + \sigma^-(u_{i+1}^{n+1})\Big) : \epsilon(v_u)\, d\Omega = \int_\Omega f(\alpha^{n+1})\Big(g(d_i^{n+1})\ \sigma_t^+(T^{n+1}) + \sigma_t^-(T^{n+1})\Big) : \epsilon(v_u)\, d\Omega \\ + \int_\Omega \Big(1 - f(\alpha^{n+1})\Big) p_L \mathbb{I} : \epsilon(v_u)\, d\Omega + \int_\Omega \rho b^*\ v_u\, d\Omega + \int_{\partial_N \Omega} t^* v_u\, d\partial_N \Omega\end{aligned} \tag{33}$$

or solve the problem in matrix form:

$$K_{u,i}^{n+1}(d_i^{n+1}, \alpha^{n+1})\ u_{i+1}^{n+1} = L_{u,i}^{n+1}(d_i^{n+1}, T^{n+1}, \alpha^{n+1}) \tag{34}$$

Next, upon solving this linear system, the new history field can be computed using its definition (eq. 13):

$$\mathcal{H}_{i+1}^{n+1} = \max\left(\mathcal{H}_i^{n+1}, \psi_{0,i+1}^{+,n+1}(u_{i+1}^{n+1})\right) \tag{35}$$

Finally, the damage variable d_{i+1}^{n+1} is computed using the history field $\mathcal{H}_{i+1}^{n+1}$, resolving the damage equation:

$$\int_\Omega \frac{2G_c l_r}{c_0}\ \nabla d_{i+1}^{n+1}\ \nabla v_d\, d\Omega + \int_\Omega \left(\frac{2G_c}{c_0 l_r} + 2f(\alpha^{n+1})\mathcal{H}_{i+1}^{n+1}\right) d_{i+1}^{n+1}\ v_d\, d\Omega = \int_\Omega 2f(\alpha^{n+1})\mathcal{H}_{i+1}^{n+1}\ v_d\, d\Omega \tag{36}$$

which in matrix form translates into:

$$\Big(K_d + A_{d,i+1}^{n+1}(\alpha^{n+1}, \mathcal{H}_{i+1}^{n+1})\Big) d_{i+1}^{n+1} = L_{d,i+1}^{n+1}(\alpha^{n+1}, \mathcal{H}_{i+1}^{n+1}) \tag{37}$$

These three steps are repeated until convergence. The convergence is reached when $||d_{i+1}^{n+1} - d_i^{n+1}||_\infty < \eta_{stag}$ where η_{stag} is a small number (in the range of 10^{-3} here).

This formulation will be used for the rest of the paper. However, the question might be whether the formulation of the liquid-solid interaction is ideal regarding the numerical modeling, or whether another expression of the damage equation is preferable. In the existing setup, the mixture law $f(\alpha^{n+1})$ is applied to the history function $\mathcal{H}_{i+1}^{n+1}$ outside its definition, resulting in the first term of the equation's right-hand side (eq. 36) being $2f(\alpha^{n+1})\mathcal{H}_{i+1}^{n+1}$.

One initial alternative idea could involve integrating the mixture law $f(\alpha^{n+1})$ into the definition of the history function $\mathcal{H}_{i+1}^{n+1}$ itself. In this revised definition, $\mathcal{H}_{i+1}^{n+1}$ would transform to: $\mathcal{H}_{i+1}^{n+1} = f(\alpha^{n+1}) \max\left(\mathcal{H}_i^{n+1}, \psi_{0,i+1}^{+,n+1}(u_{i+1}^{n+1})\right)$. Consequently, solving the discretized former damage equation (eq. 9) in the whole domain would be necessary. From a physical perspective, this formulation presents advantages. As ice melts, the history function resets to zero. With refreezing, the water reverts to ice, effectively "healing" the solid phase. Consequently, the solid can incur damage anew, akin to its initial state. However, the original concept of the history function $\mathcal{H}$ introduced by Miehe et al. [40] must adhere to the Karush-Kuhn-Tucker (KKT) conditions, notably $\dot{\mathcal{H}} \geq 0$. Integrating the mixture law $f(\alpha^{n+1})$ within

the history function definition contradicts this KKT condition. Additionally, the scenario of refreezing constitutes a specialized case of de-icing, which falls beyond the scope of this paper.

Another perspective on the damage issue involves viewing melting as damage to the solid phase. Accordingly, the approach would entail solving the initial discretized damage equation across the entire domain Ω. Wherever the liquid fraction α^{n+1} exceeds the damage value d^n, the damage is set equal to the liquid fraction, essentially considering all liquid phase as damaged. This formulation offers advantages in damage representation, particularly within the diffuse zone. However this process requires direct modification of the damage field value. Certain areas of the domain would therefore only be impacted by this change and no longer by the variational formulation. This choice would raise a number of mathematical questions not addressed in this paper.

Of the various tests carried out by the authors of this paper, the formulation initially presented seemed to be the most suitable numerically, the others not allowing convergence of the numerical solver or giving results which did not seem physically correct. Algorithm 1 summarizes the whole solving procedure.

Algorithm 1 Solving algorithm at time interval $[t^n, t^{n+1}]$

Require: Solutions of temperature field T^n (and by extension the enthalpy field h^n and the liquid fraction field α^n), the displacement field u^n, the damage field d^n and the history field $\mathcal{H}^n$

Ensure: Input fields at time t^{n+1}

Set $i = 0$, $\eta_T = 10^{-9}$, $\eta_{stag} = 10^{-3}$

Set $u_0^{n+1} \leftarrow u^n$, $d_0^{n+1} \leftarrow d^n$, $\mathcal{H}_0^{n+1} \leftarrow \mathcal{H}^n$

Compute h^{n+1} through Newton-Raphson algorithm until $||R^{n+1}||_\infty < \eta_T$ ▷ (eq.32)

Compute T^{n+1} and α^{n+1} using h^{n+1} ▷ (eq.18 and eq.21)

while $||d_{i+1}^{n+1} - d_i^{n+1}||_\infty \geq \eta_{stag}$ **do**

    Fix d_i^{n+1} and compute u_{i+1}^{n+1} ▷ (eq.34)

    Compute $\mathcal{H}_{i+1}^{n+1}$ using u_{i+1}^{n+1} ▷ (eq.35)

    Compute d_{i+1}^{n+1} using $\mathcal{H}_{i+1}^{n+1}$ ▷ (eq.37)

    $i \leftarrow i + 1$

end while

V. Benchmark tests and numerical examples

As the models are implemented, it is important to ensure that the proposed modeling correctly represents the expected phenomena. This section presents some tests carried out to validate the various models and their implementation in the simulation code.

A. Shear test

To verify the implementation of the PFM, the shear test is a popular benchmark test in the phase-field community. Presented in Fig.5, it consists in a square of $1mm \times 1mm$ of solid material with an initial crack running from one of its sides to its center. One of the side is fixed, while a shear displacement is applied to the opposite side. The imposed displacement is increased by $10^{-5}mm$ at each time iteration. The damage field for different displacement values is shown in Fig.6.

As expected, the crack propagated through the solid until it reaches a stage where the damage in the lower right-hand corner cannot change. These results are similar to those found in the literature [38, 40, 42], assessing our numerical implementation.

B. Melting test

At the same time as the PFM is validated, the thermal modeling is also validated. For this, a simple Stefan's problem is solved. This involves melting a semi-infinite plate initially made of a solid material where a temperature (higher than the melting point of the material) is imposed on its finished side. The heat would then diffuse into the solid, causing it to melt. Stefan's problem involves determining the position of the melting front x_Γ and the temperature field T in the domain over time, which in reality consists of solving a uni-axial problem. A scheme of the problem is presented in Fig.7. For this validation test, the case of ice at $T_S = 250K$ melting into water at $T_L = 300K$ during $15s$ is considered.

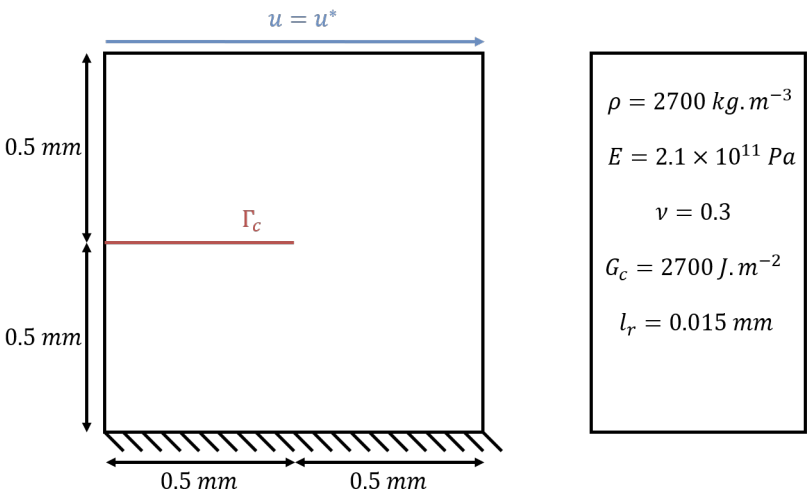

Fig. 5 Schematic of the shear test and material properties

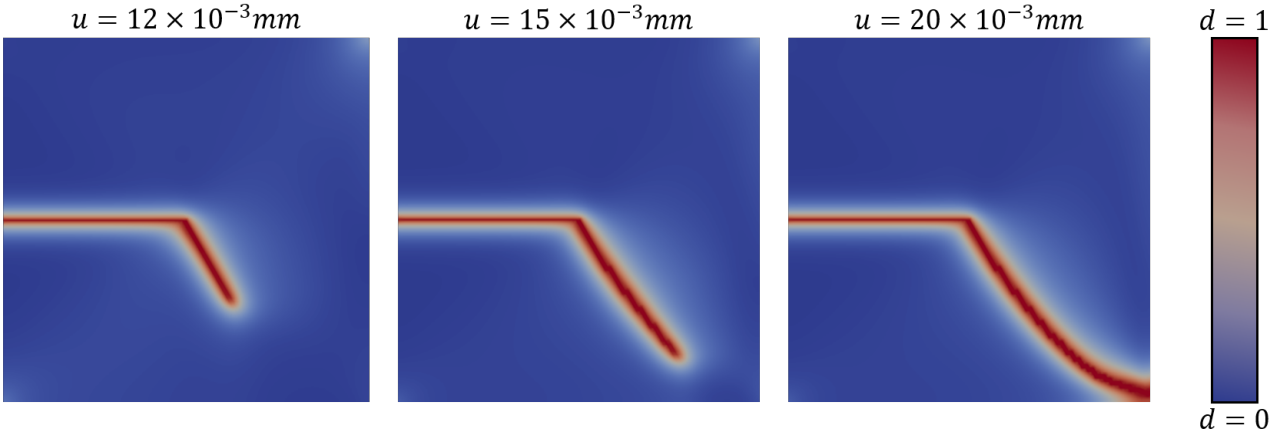

Fig. 6 Numerical result of the damage field for the shear test for different displacement values: $12 \times 10^{-3} mm$**,** $15 \times 10^{-3} mm$ **and** $20 \times 10^{-3} mm$

The thermal conductivities ($k_l = 0.6 W.m^{-1}.K^{-1}$ and $k_s = 2.3 W.m^{-1}.K^{-1}$) and capacities ($c_l = 4187 J.kg^{-1}.K^{-1}$ and $c_s = 2108 J.kg^{-1}.K^{-1}$) of water and ice, and the latent heat of melting ($L_{fus} = 3.33 \times 10^5 J.kg^{-1}$) are taken independent of the temperature.

The position of the melting front and the temperature field at times $1s$, $5s$, $10s$ and $15s$ are displayed in Fig.8. It is seen that the melting front moves over time, transforming the ice into water. A comparison between the numerical and analytical results for the position of the melting front x_Γ and the temperature field T are presented in Fig.9 and Fig.10 respectively. The analytical solution of Stefan's problem can be found in [24].

The chosen model for the thermal subproblem seems to correctly represent the melting process. The temperature and liquid fraction fields are well reconstructed from the enthalpy field over time.

C. Quenching test

Once the PFM and thermal models have been validated, the thermo-mechanical model can also be tested. A good benchmark test for the verification of such a model is that of quenching. It consists of a piece of ceramic heated at $T = 600K$, then immersed in an oil bath at $T = 300K$. After being dropped, the material is removed from the oil bath. During this process, a series of cracks appeared on the edges of the solid due to the thermal shock of quenching. Even if there is no phase change in this benchmark test, the thermal model can still be used for this simulation. The results of the simulation are presented in Fig.11.

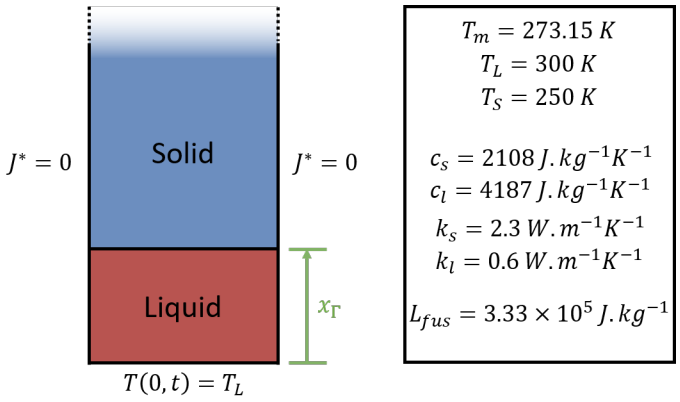

Fig. 7 Schematic of the Stefan's problem and materials properties

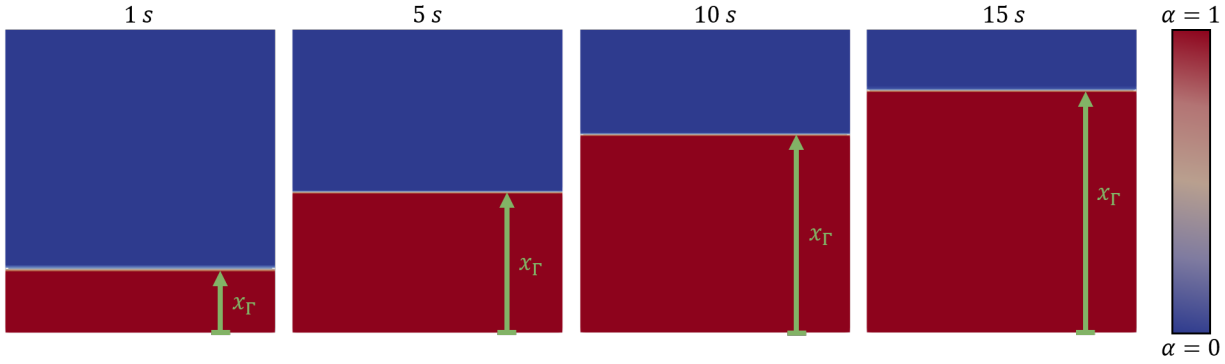

Fig. 8 Numerical results of the liquid fraction field for the Stefan's problem at different times: $1s$, $5s$, $10s$ and $15s$

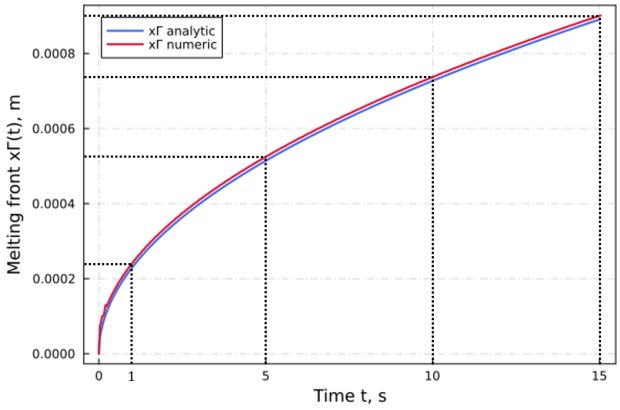

Fig. 9 Comparison of the position of the melting front x_Γ between numerical and analytical results over time

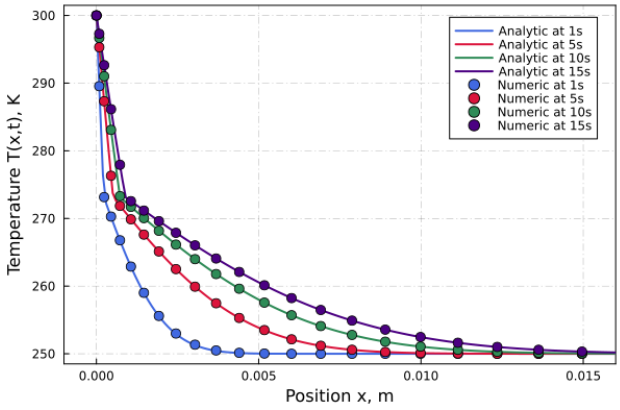

Fig. 10 Comparison of temperature field T between numerical and analytical results for different times

There appears to be a good correlation between this numerical simulation and experimental data [43] or numerical results found in literature [44, 45]. The crack patterns seems to be quite the same as the experimental case, both qualitatively and quantitatively. From this result, it is concluded that the thermo-mechanical model is validated.

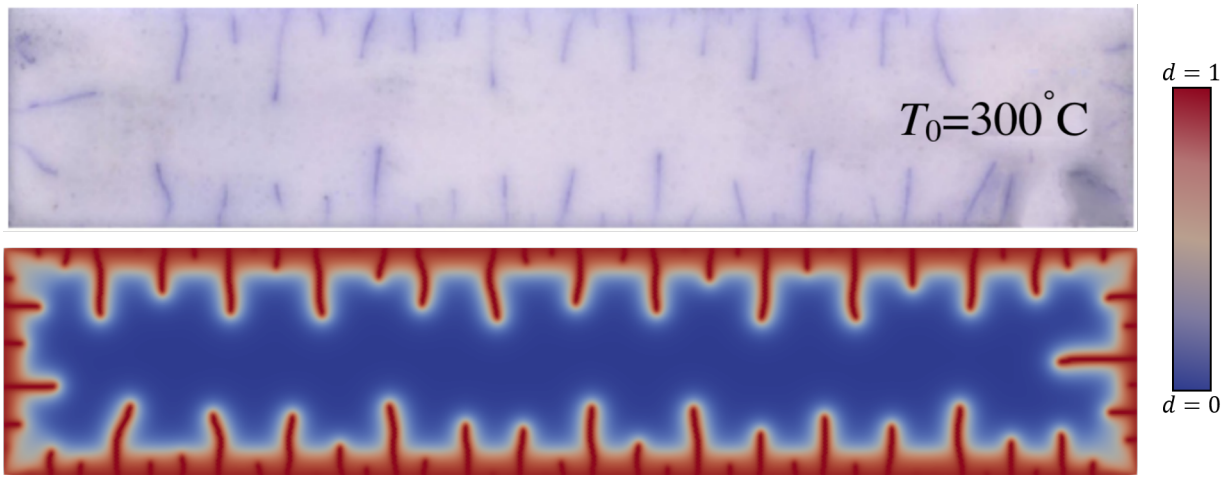

Fig. 11 Damage field d from numerical simulation of the quenching test, in comparison with an experiment (experimental figure from Jiang et al. [43])

D. Ice shape on flat plate test case

Finally, to challenge the entire model, a simple test case of an ice shape attached to a flat plate is realized. This test case serves mainly to illustrate the capabilities of the model, and also to verify the behaviour hypotheses described in part II.A and on Fig. 2. The ice shape, illustrated in Fig.12, is characterized by a length $L_t = 31.225mm$ and a height $e_{ice} = 3mm$. The ElectroThermal Ice Protection System (ETIPS) is set to activated over a distance L_f.

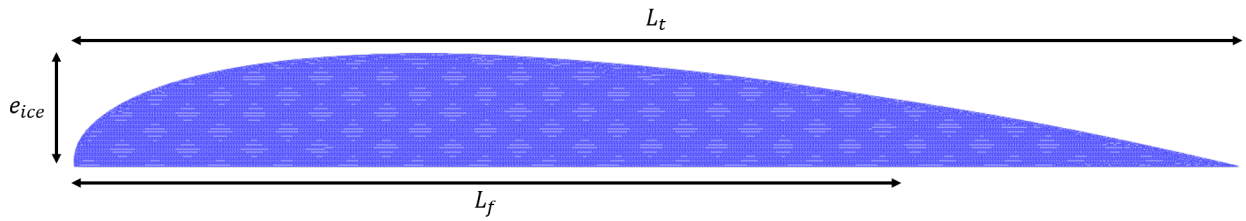

Fig. 12 Flat plate test case configuration

The goal here is to determine the percentage $\frac{L_f}{L_t}$ required to melt in order to generate and propagate a crack leading to shedding. The length L_f is increased at each case to find the critical shedding percentage value. A numerical comparaison will be made with the results of Bennani's model [15] and an experimental comparaison with the works of Enache et al. [20, 21] will permit to asses the model presented in this paper. For this test case, the ice block is discretized into about 30000 triangular elements and the algorithm presented previously is used to solve the equations.

In the simulation results presented below, two parameters are varied in order to observe their influence: the external temperature (and by extension the inital ice temperature) which were taken at 268.15 and 263.15 K, and the ETIPS heat flux which were taken at 12.5 and 19 kW.m^{-2}. The Young's modulus of ice is chosen at $E = 9.3$ GPa and the Poisson's ratio at $\nu = 0.325$. The simulation runs for ten seconds which is a typical de-icing cycle time. The ETIPS is set to heat initially a percentage $\frac{L_f}{L_t} = 65\%$. This value is increased by 1% at each simulation until the critical percentage length shedding is reached.

On Fig. 13, two simulation results for $\frac{L_f}{L_t} = 70\%$ and 71% are presented. As expected, the pressure difference between the liquid layer and the external pressure creates an uplifting force which conducts to the nucleation and the propagation of a crack in the ice block (a). However, if the length L_f is too small, the forces in the ice are not sufficient to propagate the crack (b). These results are in agreement with the results of Bennani's works with a slight difference of 2% less on L_f. This discrepancy can be explained by the fact that Bennani's model did not remove the molten zone from the mesh, where the displacement and damage equations are solved. Moreover, the mesh used and the regularised length l_r was not the same. As the liquid layer grows, the thickness of the ice block decreases, thus increasing stresses

in the material until a crack appears and propagates. Futhermore, thermoelastic effects are now taken into account, which leads to an acceleration of the shedding phenomenon.

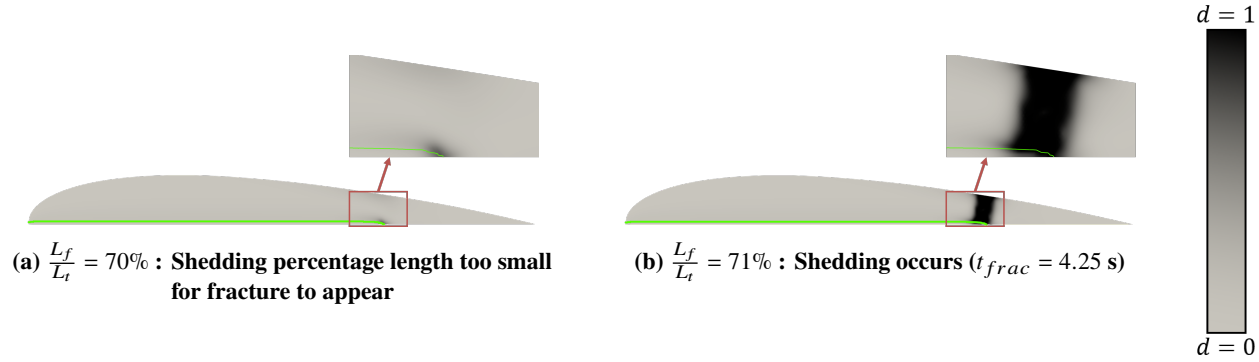

(a) $\frac{L_f}{L_t} = 70\%$ **: Shedding percentage length too small for fracture to appear**

(b) $\frac{L_f}{L_t} = 71\%$ **: Shedding occurs** ($t_{frac} = 4.25$ **s**)

Fig. 13 Simulation results for two different percentages $\frac{L_f}{L_t}$ **for** $T_0 = 268$ **K and** $q^* = 19$ **kW.m**$^{-2}$**, the green line represents the liquid-solid interface** ($\alpha = 0.5$)

Now that the critical shedding length has been computed, it is interesting to analyze the influence of increasing this length beyond the critical value. An increase in the melted length is expected to accelerate the shedding process and reduce the amount of ice that remains attached. In Fig. 14, four different ice shedding simulations are presented, ranging from 71% to 74%, as well as the associated shedding times. The initial temperature is set at $T_0 = 268$ K, and the heat flux is $q^* = 12.5$ kW.m^{-2}.

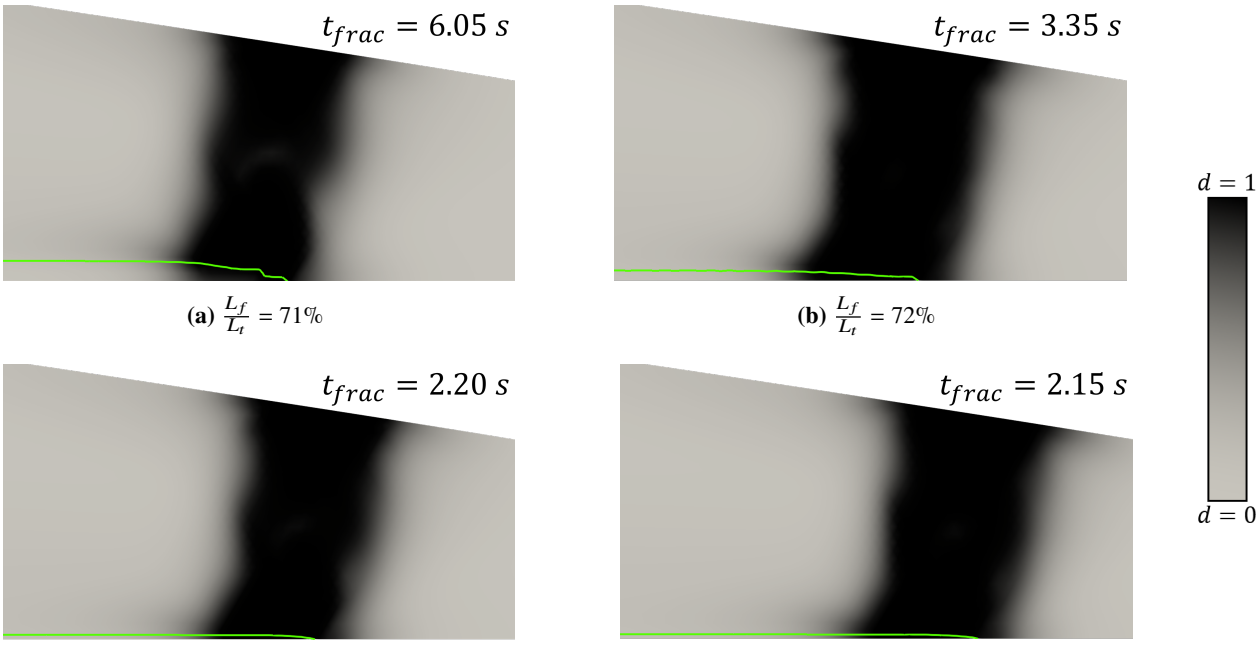

(a) $\frac{L_f}{L_t} = 71\%$

(b) $\frac{L_f}{L_t} = 72\%$

(c) $\frac{L_f}{L_t} = 73\%$

(d) $\frac{L_f}{L_t} = 74\%$

Fig. 14 Influence of $\frac{L_f}{L_t}$ **percentage on ice shedding simulation at** $T_0 = 268$ **K and** $q^* = 12.5$ **kW.m**$^{-2}$

The simulations in Fig.14 reveal a clear trend: as L_f increases from 71% to 74%, the associated shedding times decrease significantly. This confirms the prediction that increasing L_f would lead to faster shedding and a reduction in the amount of ice remaining attached. This effect can be attributed to the expansion of the heat-exposed zone, which promotes the formation of a larger liquid layer. This liquid layer reduces the contact between the ice and the wing

surface, thereby lowering the mechanical resistance to shedding. Additionally, the broader pressure distribution zone created by the expanded melt layer aids in overcoming the cohesive forces within the ice, making the detachment process more effective. As a result, the additional melted length facilitates the detachment process, allowing ice to shed more efficiently. It appears, however, that increasing the melting length L_f leads to a limit in fracture time, probably the time needed for the liquid layer to appear. All these observations are in agreement with the experimental results of Enache et al. [20, 21]. Indeed, they have noticed that increasing the melting length L_f reduces the fracture time until reaching a time limit and decreases the ammount of ice remaining.

The influence of the initial temperature T_0 on the shedding process is also noteworthy. In this scenario, the percentage $\frac{L_f}{L_t}$ is fixed at 72% and the heat flux remains constant at $q^* = 12.5$ kW.m^{-2}. The results are presented Fig.15 for two temperatures: 263 K and 268 K.

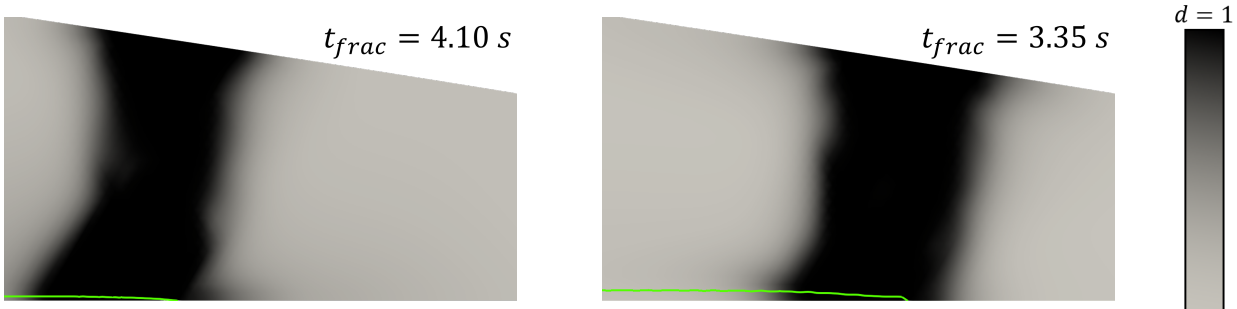

(a) $T_0 = 263$ **K** **(b)** $T_0 = 268$ **K**

Fig. 15 Influence of the initial temperature T_0 on ice shedding simulation at $\frac{L_f}{L_t} = 72\%$ K and $q^* = 12.5$ kW.m^{-2}

As expected, the liquid layer develops more slowly at $T_0 = 263$ K compared to $T_0 = 268$ K due to the lower initial temperature. This slower development results in a smaller pressure distribution zone in the first case. One might anticipate that the liquid layer would need to reach the same extent as in the second case before the shedding process could be triggered. However, observations indicate that this is not the case. While the scenario at $T_0 = 263$ K requires a longer time to initiate shedding and is in line with the experimental work of Enache et al. [21], fracture still begins with a smaller liquid layer. This phenomenon can be explained by the greater temperature gradient in the first case, which results in stronger thermoelastic effects. These effects generate a crack further upstream in the ice block, thereby facilitating the shedding process even with a smaller liquid layer. This also can be justified by a quick calculation. The thermal stress must be of the order of magnitude of $\sigma_t = E\,\beta\,(T - T_0)$. When the temperature in the ice reaches the melting point, the temperature difference should be around 10 K. Thus the thermal stress becomes approximately $\sigma_t \approx 4.5$ MPa which is the same order as the tensile strength of ice concluding that thermoelastic effects cannot be neglected for the ice shedding modeling.

This test case is fairly basic, but it reveals some important external parameters governing the shedding phenomenon such as the ETIPS activation length or the external temperature (and consequently the initial ice block temperature). Simulations have shown that the extention of the melting length L_f decreases the quantity of ice remaining on the wing and lowers the shedding time until a limit value is reached. The initial temperature also have a significant impact on results. As this temperature decreases, thermoelastic effects become more and more significant, allowing crack generation and propagation even if the liquid layer is smaller. This test case also showed that the algorithm's behavior tends to obtain results similar to the numerical works of Bennani [15] and the experimental results of Enache et al. [20, 21]. However, some work remains to be done and a more in-depth analysis of the model will provide a better understanding of its application.

VI. Conclusion

This paper introduces a novel liquid-solid thermo-mechanical phase-field fracture model for electrothermal de-icing applications. Initially, it provides a comprehensive overview of existing models addressing the various phenomena involved in ice shedding, followed by a detailed justification for the models chosen in this study. Starting with a classical thermo-mechanical fracture model, a liquid-solid interaction is incorporated to represent the influence of a liquid layer

on the ice block, utilizing a mixture law method. The implications of this integration on the governing equations are analyzed, along with an elaboration on the numerical implementation and algorithm.

A test case of an ETIPS (ElectroThermal Ice Protection System) for an ice shape on a flat plate was conducted to study the algorithm's behavior in an electrothermal de-icing context. Simulations demonstrated that the melting length and the external temperature are critical parameters influencing ice shedding. The numerical results suggest an optimal range for the melting length, beyond which further increases yield diminishing returns. It was also shown that a lower initial temperature can lead to a more strategic application of heat, exploiting the temperature gradient to maximize the thermoelastic effects. Therefore, by optimizing the melting length, fine-tuning the heat flux, and targeting specific areas of the ice, such systems could improve the de-icing process's effectiveness across various environmental conditions. Through a parametric analysis, this type of simulation can also help better apprehend the material properties of ice, which are still not fully understanded nowadays.

Ice shedding is a complex phenomenon involving numerous multiphysical aspects, making it a challenging area of study. The model presented in this paper makes several critical hypotheses, including assuming a static liquid layer and resolving the mechanical part as stationary. These simplifications, although necessary for the initial development of the model, highlight the need for further refinement. An in-depth study focusing on this model will be the subject of a future paper, aiming to provide a more robust understanding of ice shedding modeling. Very few data is avaible in the literature, particularly concerning the mechanisms of ice block cracking, which is essential for validating and improving theoretical models. Future research should prioritize gathering extensive experimental data to enhance model accuracy and explore the nuanced interplay of physical forces involved in ice shedding. Ultimately, advancing this research could lead to more effective strategies for managing ice accumulation in various applications, especially in the aeronautical field.

Acknowledgments

This work is a collaboration between ONERA (Office national d'études et de recherches aérospatiales) and ISAE (Institut supérieur de l'aéronautique et de l'espace) SUPAERO. It is supported by a French government grant managed by the Agence Nationale de la Recherche under the Programme d'Investissements d'Avenir (ANR-17-EURE-0005), and ONERA. Authors gratefully acknowledge them for their support.

References

[1] Caroll, T., and McAvoy, W. H., "The formation of ice upon airplanes in flight," Technical Notes 313, Langley Memorial Aeronautical Laboratory, Washigton, Aug. 1929. URL https://ia800501.us.archive.org/11/items/nasa_techdoc_19930081134/19930081134.pdf.

[2] Geer, W. C., "An analysis of the problem of ice on airplanes," *Journal of the Aeronautical Sciences*, Vol. 6, No. 11, 1939, pp. 451–459. https://doi.org/10.2514/8.941, URL https://arc.aiaa.org/doi/10.2514/8.941.

[3] Gent, R. W., Dart, N. P., and Cansdale, J. T., "Aircraft icing," *Philosophical Transactions of the Royal Society of London. Series A: Mathematical, Physical and Engineering Sciences*, Vol. 358, No. 1776, 2000, pp. 2873–2911. https://doi.org/10.1098/rsta.2000.0689, URL https://royalsocietypublishing.org/doi/10.1098/rsta.2000.0689, publisher: Royal Society.

[4] Gowan, W. H., and Mulholland, D. R., "Effectiveness of thermal-pneumatic airfoil ice protection system," Research Memorandum NACA-RM-E50K10A, NACA, Lewis Flight Propulsion Laboratory, Cleveland, Ohio, Apr. 1951. URL https://ntrs.nasa.gov/citations/19810068604.

[5] Zumwalt, G. W., Schrag, R. L., Bernhart, W. D., and Friedberg, R. A., "Analyses and tests for design of an electro-impulse de-icing system," Interim Report 174919, Lewis Research Center, NASA, Wichita State University, Wichita, Kansas, May 1985. URL https://ntrs.nasa.gov/citations/19860017796.

[6] Albright, A., "A summary of NASA's research on the fluid ice protection system," *23rd Aerospace Sciences Meeting*, American Institute of Aeronautics and Astronautics, Reno, NV, U.S.A., 1985. https://doi.org/10.2514/6.1985-467, URL https://arc.aiaa.org/doi/10.2514/6.1985-467.

[7] Theodorsen, T., and Clay, W. C., "Ice prevention on aircraft by means of engine exhaust heat and a technical study of heat transmission from a clark Y airfoil," Technical Notes 403, Langley Memorial Aeronautical Laboratory, Langley Field, Hampton, Virginia, Jan. 1931. URL https://ntrs.nasa.gov/api/citations/19930091477/downloads/19930091477.pdf.

[8] Bennani, L., Villedieu, P., Salaun, M., and Trontin, P., "Numerical simulation and modeling of ice shedding: Process initiation," *Computers & Structures*, Vol. 142, 2014, pp. 15–27. https://doi.org/10.1016/j.compstruc.2014.06.001, URL https://www.sciencedirect.com/science/article/pii/S0045794914001333.

[9] Henry, R., "Development of an electrothermal de-icing/anti-icing model," *30th Aerospace Sciences Meeting and Exhibit*, 1992, p. 9. https://doi.org/10.2514/6.1992-526, URL https://arc.aiaa.org/doi/10.2514/6.1992-526.

[10] Scavuzzo, R. J., Chu, M. L., and Ananthaswamy, V., "Influence of aerodynamic forces in ice shedding," *Journal of Aircraft*, Vol. 31, No. 3, 1994, pp. 526–530. https://doi.org/10.2514/3.46525, URL https://arc.aiaa.org/doi/10.2514/3.46525, publisher: American Institute of Aeronautics and Astronautics.

[11] Zhang, S., El Kerdi, O., Khurram, R. A., and Habashi, W. G., "FEM analysis of in-flight ice break-up," *Finite Elements in Analysis and Design*, Vol. 57, 2012, pp. 55–66. https://doi.org/10.1016/j.finel.2012.03.005, URL https://www.sciencedirect.com/science/article/pii/S0168874X1200056X.

[12] Wright, W., "User's manual for LEWICE Version 3.2," User's Manual E-15537, NASA, Cleveland, Ohio, Nov. 2008. URL https://ntrs.nasa.gov/citations/20080048307.

[13] Reid, T., Baruzzi, G. S., and Habashi, W. G., "FENSAP-ICE: Unsteady conjugate heat transfer simulation of electrothermal de-icing," *Journal of Aircraft*, Vol. 49, No. 4, 2012, pp. 1101–1109. https://doi.org/10.2514/1.C031607, URL https://arc.aiaa.org/doi/10.2514/1.C031607.

[14] Trontin, P., Kontogiannis, A., Blanchard, G., and Villedieu, P., "Description and assessment of the new ONERA 2D icing suite IGLOO2D," *AIAA AVIATION Forum*, Denver, Colorado, 2017. https://doi.org/10.2514/6.2017-3417, URL https://arc.aiaa.org/doi/10.2514/6.2017-3417.

[15] Bennani, L., "Modélisation bidimensionnelle de systèmes électrothermiques de protection contre le givre," Ph.D. thesis, Toulouse III - Paul Sabatier, Toulouse, 2014. URL http://www.theses.fr/2014ESAE0037.

[16] Ruan, H., Rezaei, S., Yang, Y., Gross, D., and Xu, B.-X., "A thermo-mechanical phase-field fracture model: Application to hot cracking simulations in additive manufacturing," *Journal of the Mechanics and Physics of Solids*, Vol. 172, 2023, p. 105169. https://doi.org/10.1016/j.jmps.2022.105169, URL https://www.sciencedirect.com/science/article/pii/S0022509622003453.

[17] Yeo, H., and Ki, H., "A unified momentum equation approach for computing thermal residual stresses during melting and solidification," *Computer Physics Communications*, Vol. 224, 2018, pp. 230–244. https://doi.org/10.1016/j.cpc.2017.10.013, URL https://www.sciencedirect.com/science/article/pii/S0010465517303533.

[18] Sun, X., Duddu, R., and Hirshikesh, H., "A poro-damage phase field model for hydrofracturing of glacier crevasses," *Extreme Mechanics Letters*, Vol. 45, 2021, p. 101277. https://doi.org/10.1016/j.eml.2021.101277, URL https://www.sciencedirect.com/science/article/pii/S2352431621000626.

[19] Clayton, T., Duddu, R., Siegert, M., and Martínez-Pañeda, E., "A stress-based poro-damage phase field model for hydrofracturing of creeping glaciers and ice shelves," *Engineering Fracture Mechanics*, Vol. 272, 2022, p. 108693. https://doi.org/10.1016/j.engfracmech.2022.108693, URL https://www.sciencedirect.com/science/article/pii/S0013794422004167.

[20] Enache, A., Bernay, B., Glabeke, G., Planquart, P., and van Beeck, J., "Ice shedding phenomenon: an experimental and numerical investigation," *AIAA AVIATION 2020 FORUM*, American Institute of Aeronautics and Astronautics, Virtual Event, 2020. https://doi.org/10.2514/6.2020-2817, URL https://arc.aiaa.org/doi/abs/10.2514/6.2020-2817.

[21] Enache, A., Bernay, B., Glabeke, G., Planquart, P., van Beeck, J., and Hendrick, P., "Electrothermal ice protection systems de-icing: An experimentally validated idealized ice shedding model," *AIAA Journal*, Vol. 61, No. 6, 2023, pp. 2526–2551. https://doi.org/10.2514/1.J062256, URL https://doi.org/10.2514/1.J062256.

[22] Prosperetti, A., and Tryggvason, G. (eds.), *Computational methods for multiphase flow*, Cambridge University Press, Cambridge, 2007. https://doi.org/10.1017/CBO9780511607486, URL https://www.cambridge.org/core/books/computational-methods-for-multiphase-flow/B2BD97E62BA30AA80779E5E54B47A5B4.

[23] Bennani, L., Trontin, P., and Radenac, E., "Numerical simulation of an electrothermal ice protection system in anti-icing and deicing mode," *Aerospace*, Vol. 10, No. 1, 2023, p. 75. https://doi.org/10.3390/aerospace10010075, URL https://www.mdpi.com/2226-4310/10/1/75.

[24] Alexiades, V., and Solomon, A., *Mathematical modeling of melting and freezing processes*, Routledge, New York, 1992. https://doi.org/10.1201/9780203749449.

[25] Santillán, D., Juanes, R., and Cueto-Felgueroso, L., "Phase field model of fluid-driven fracture in elastic media: Immersed-fracture formulation and validation with analytical solutions," *Journal of Geophysical Research: Solid Earth*, Vol. 122, No. 4, 2017, pp. 2565–2589. https://doi.org/10.1002/2016JB013572, URL http://doi.wiley.com/10.1002/2016JB013572.

[26] Griffith, A. A., "The phenomena of rupture and flow in solids," *Philosophical Transactions of the Royal Society of London Series A*, Vol. 221, 1921, pp. 163–198. https://doi.org/10.1098/rsta.1921.0006, URL https://ui.adsabs.harvard.edu/abs/1921RSPTA.221..163G.

[27] Kachanov, L. M., "Rupture time under creep conditions," *International Journal of Fracture*, Vol. 97, 1999, pp. 11–18. https://doi.org/10.1023/A:1018671022008, URL https://link.springer.com/article/10.1023/A:1018671022008.

[28] Frémond, M., and Nedjar, B., "Damage, gradient of damage and principle of virtual power," *International Journal of Solids and Structures*, Vol. 33, No. 8, 1996, pp. 1083–1103. https://doi.org/10.1016/0020-7683(95)00074-7, URL https://www.sciencedirect.com/science/article/pii/0020768395000747.

[29] Peerlings, R. H. J., De Borst, R., Brekelmans, W. a. M., and De Vree, J. H. P., "Gradient enhanced damage for quasi-brittle materials," *International Journal for Numerical Methods in Engineering*, Vol. 39, No. 19, 1996, pp. 3391–3403. https://doi.org/10.1002/(SICI)1097-0207(19961015)39:19<3391::AID-NME7>3.0.CO;2-D, URL https://onlinelibrary.wiley.com/doi/abs/10.1002/%28SICI%291097-0207%2819961015%2939%3A19%3C3391%3A%3AAID-NME7%3E3.0.CO%3B2-D.

[30] Leguillon, D., "Strength or toughness? A criterion for crack onset at a notch," *European Journal of Mechanics - A/Solids*, Vol. 21, No. 1, 2002, pp. 61–72. https://doi.org/10.1016/S0997-7538(01)01184-6, URL https://www.sciencedirect.com/science/article/pii/S0997753801011846.

[31] Dugdale, D. S., "Yielding of steel sheets containing slits," *Journal of the Mechanics and Physics of Solids*, Vol. 8, No. 2, 1960, pp. 100–104. https://doi.org/10.1016/0022-5096(60)90013-2, URL https://www.sciencedirect.com/science/article/pii/0022509660900132.

[32] Barenblatt, G. I., "The mathematical theory of equilibrium cracks in brittle fracture," *Advances in Applied Mechanics*, Vol. 7, 1962, pp. 55–129. https://doi.org/10.1016/S0065-2156(08)70121-2, URL https://www.sciencedirect.com/science/article/pii/S0065215608701212.

[33] Bourdin, B., Francfort, G. A., and Marigo, J.-J., "Numerical experiments in revisited brittle fracture," *Journal of the Mechanics and Physics of Solids*, Vol. 48, No. 4, 2000, pp. 797–826. https://doi.org/10.1016/S0022-5096(99)00028-9, URL https://www.sciencedirect.com/science/article/pii/S0022509699000289.

[34] Francfort, G. A., and Marigo, J. J., "Revisiting brittle fracture as an energy minimization problem," *Journal of the Mechanics and Physics of Solids*, Vol. 46, No. 8, 1998, pp. 1319–1342. https://doi.org/10.1016/S0022-5096(98)00034-9, URL https://www.sciencedirect.com/science/article/pii/S0022509698000349.

[35] Wu, J.-Y., Nguyen, V. P., Thanh Nguyen, C., Sutula, D., Bordas, S., and Sinaie, S., "Phase field modelling of fracture," *Advances in Applied Mechanics*, Vol. 53, 2019, pp. 1–183. https://doi.org/10.1016/bs.aams.2019.08.001, URL https://www.sciencedirect.com/science/article/pii/S0065215619300134.

[36] Borden, M. J., Verhoosel, C. V., Scott, M. A., Hughes, T. J. R., and Landis, C. M., "A phase-field description of dynamic brittle fracture," *Computer Methods in Applied Mechanics and Engineering*, Vol. 217-220, 2012, pp. 77–95. https://doi.org/10.1016/j.cma.2012.01.008, URL https://www.sciencedirect.com/science/article/pii/S0045782512000199.

[37] Lancioni, G., and Royer-Carfagni, G., "The variational approach to fracture mechanics. A practical application to the french Panthéon in Paris," *Journal of Elasticity*, Vol. 95, No. 1, 2009, pp. 1–30. https://doi.org/10.1007/s10659-009-9189-1, URL https://doi.org/10.1007/s10659-009-9189-1.

[38] Wu, J.-Y., "A unified phase-field theory for the mechanics of damage and quasi-brittle failure," *Journal of the Mechanics and Physics of Solids*, Vol. 103, 2017, pp. 72–99. https://doi.org/10.1016/j.jmps.2017.03.015, URL https://www.sciencedirect.com/science/article/pii/S0022509616308341.

[39] Pham, K., Amor, H., Marigo, J.-J., and Maurini, C., "Gradient damage models and their use to approximate brittle fracture," *International Journal of Damage Mechanics*, Vol. 20, No. 4, 2011, pp. 618–652. https://doi.org/10.1177/1056789510386852, URL https://doi.org/10.1177/1056789510386852, publisher: SAGE Publications Ltd STM.

[40] Miehe, C., Hofacker, M., and Welschinger, F., "A phase field model for rate-independent crack propagation: Robust algorithmic implementation based on operator splits," *Computer Methods in Applied Mechanics and Engineering*, Vol. 199, No. 45, 2010, pp. 2765–2778. https://doi.org/10.1016/j.cma.2010.04.011, URL https://www.sciencedirect.com/science/article/pii/S0045782510001283.

[41] Blanchard, G., bmxam, and lokmanb, "bcube-project/Bcube.jl: v0.1.11," , Jun. 2024. https://doi.org/10.5281/zenodo.12097781, URL https://zenodo.org/records/12097781.

[42] Ambati, M., Gerasimov, T., and De Lorenzis, L., "A review on phase-field models of brittle fracture and a new fast hybrid formulation," *Computational Mechanics*, Vol. 55, No. 2, 2015, pp. 383–405. https://doi.org/10.1007/s00466-014-1109-y, URL https://doi.org/10.1007/s00466-014-1109-y.

[43] Jiang, C. P., Wu, X. F., Li, J., Song, F., Shao, Y. F., Xu, X. H., and Yan, P., "A study of the mechanism of formation and numerical simulations of crack patterns in ceramics subjected to thermal shock," *Acta Materialia*, Vol. 60, No. 11, 2012, pp. 4540–4550. https://doi.org/10.1016/j.actamat.2012.05.020, URL https://www.sciencedirect.com/science/article/pii/S1359645412003308.

[44] Mandal, T. K., Nguyen, V. P., Wu, J.-Y., Nguyen-Thanh, C., and de Vaucorbeil, A., "Fracture of thermo-elastic solids: Phase-field modeling and new results with an efficient monolithic solver," *Computer Methods in Applied Mechanics and Engineering*, Vol. 376, 2021, p. 113648. https://doi.org/10.1016/j.cma.2020.113648, URL https://www.sciencedirect.com/science/article/pii/S0045782520308331.

[45] Wang, T., Ye, X., Liu, Z., Liu, X., Chu, D., and Zhuang, Z., "A phase-field model of thermo-elastic coupled brittle fracture with explicit time integration," *Computational Mechanics*, Vol. 65, No. 5, 2020, pp. 1305–1321. https://doi.org/10.1007/s00466-020-01820-6, URL https://doi.org/10.1007/s00466-020-01820-6.